JOURNAL OF GEOPHYSICAL RESEARCH, VOL. 115, A03103, doi:10.1029/2009JA014705, 2010

Click Here for Full Article

Cosmic ray diffusion tensor throughout the heliosphere

C. Pei,[1] J. W. Bieber,[1] B. Breech,[2] R. A. Burger,[3] J. Clem,[1] and W. H. Matthaeus[1]

Received 30 July 2009; revised 14 October 2009; accepted 3 November 2009; published 30 March 2010.

[1] We calculate the cosmic ray diffusion tensor based on a recently developed model of magnetohydrodynamic (MHD) turbulence in the expanding solar wind. Parameters of this MHD model are tuned by using published observations from Helios, Voyager 2, and Ulysses. We present solutions of two turbulence parameter sets and derive the characteristics of the cosmic ray diffusion tensor for each. We determine the parallel diffusion coefficient of the cosmic rays following the method presented by Bieber et al. (1995). We use the nonlinear guiding center theory to obtain the perpendicular diffusion coefficient of the cosmic rays. We find that (1) the radial mean free path decreases from 1 to 30 AU for both turbulence scenarios; (2) after 30 AU the radial mean free path is nearly constant; (3) the radial mean free path is dominated by the parallel component before 30 AU, after which the perpendicular component becomes important; (4) the rigidity dependence of the parallel mean free path is proportional to $P^{.404}$ for one turbulence scenario and $P^{.374}$ for the other at 1 AU from 0.1 to 10 GV, but in the outer heliosphere its dependence steepens above 4 GV; and (5) the rigidity dependence of the perpendicular mean free path is very weak.

Citation: Pei, C., J. W. Bieber, B. Breech, R. A. Burger, J. Clem, and W. H. Matthaeus (2010), Cosmic ray diffusion tensor throughout the heliosphere, *J. Geophys. Res.*, *115*, A03103, doi:10.1029/2009JA014705.

1. Introduction

[2] To understand the modulation of cosmic rays, we need to know the properties of plasma turbulence throughout the heliosphere and derive the cosmic ray diffusion tensor at all locations based on observations and appropriate diffusion models. We intend eventually to employ the derived diffusion tensor in ab initio models of the solar modulation of cosmic rays [*Parhi et al.*, 2003; *Minnie*, 2006], in which the diffusion tensor is computed from first principles based on the turbulence properties. However, in the present paper we concentrate on the properties of the diffusion tensor itself.

[3] The evolution of the turbulence is governed by magnetohydrodynamic (MHD) theory which involves 16 coupled spectral equations [*Marsch and Tu*, 1989; *Zhou and Matthaeus*, 1990a]. Fortunately these equations can be simplified by applying assumptions relevant to the solar wind and a tractable set of equations was recently developed [*Zank et al.*, 1996; *Matthaeus et al.*, 1999; *Smith et al.*, 2001; *Isenberg et al.*, 2003; *Breech et al.*, 2008]. As these turbulence models become more and more sophisticated, numerical results based on these models provide better understanding of Voyager, Helios, and Omni observations of the heliocentric variation of magnetic turbulence amplitude, magnetic correlation scale, plasma temperature, and cross helicity.

[4] Although parallel diffusion of charged energetic particles appears to be well understood based upon quasi-linear theory [*Jokipii*, 1966; *Bieber et al.*, 1994], perpendicular diffusion remains a challenge. The process of perpendicular diffusion includes field line random walk, backscatter from parallel diffusion, and transfer of particles across field lines. Since the "nonlinear guiding center"(NLGC) theory considered all of these factors mentioned above [*Matthaeus et al.*, 2003], it is a promising one among other theories. One attractive feature of this theory is that the parallel mean free path is the only particle property required to determine uniquely the perpendicular mean free path. Further, the theory is consistent with key observational constraints [*Bieber et al.*, 2004] derived from Jovian electrons [*Chenette et al.*, 1977] and from Ulysess measurements of Galactic protons [*Burger et al.*, 2000].

[5] The calculation of the mean free paths is divided into two steps. First, the 2-D turbulence properties are calculated based on the turbulence model presented by *Breech et al.* [2008]. This model employs an approach developed in recent years to explain observations made by Voyager, Pioneer, and Ulysses. By specifying appropriate boundary conditions, this model provides a reasonable accounting of turbulence properties anywhere in a model heliosphere. Second, with the turbulence parameters specified, the perpendicular mean free path is calculated based on the NLGC theory for perpendicular diffusion [*Bieber et al.*, 2004] and the parallel mean free path is based on quasi-linear theory as given by *Bieber et al.* [1995].

[1]Bartol Research Institute, Department of Physics and Astronomy, University of Delaware, Newark, Delaware, USA.
[2]NASA Goddard Space Flight Center, Greenbelt, Maryland, USA.
[3]Unit for Space Physics, School of Physics, North-West University, Potchefstroom, South Africa.

Copyright 2010 by the American Geophysical Union.
0148-0227/10/2009JA014705

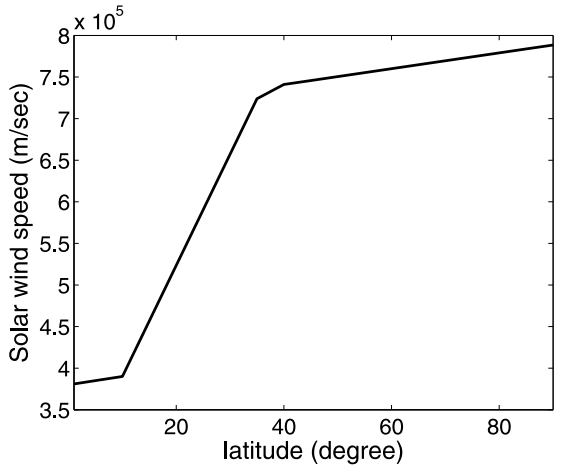

Figure 1. Solar wind speed as a function of heliographic latitude.

[6] The present work makes several major departures from prior [*Bieber et al.*, 1995; *Zank et al.*, 1998] work in this area. This is motivated by recent advances both in particle transport theory and in turbulence transport theory, and by new information on the properties of turbulence in the solar wind. The most important departures are enumerated as follows:

[7] 1. Models of turbulence transport in the solar wind have improved dramatically over the past decade. This work employs the model of *Breech et al.* [2008], which only recently became available.

[8] 2. Past turbulence transport models have tuned the model parameters by comparing them with observations of turbulence energy, correlation scale, temperature, and cross helicity. Here, we impose an additional constraint: that the turbulence model produce the correct (i.e., consensus [see *Palmer*, 1982; *Bieber et al.*, 1994]) value of the cosmic ray parallel mean free path at 1 AU. We also consider a second parameter set representing a reasonable variation from the optimal set, in order to characterize how sensitive the diffusion tensor is to the turbulence properties.

[9] 3. We assume that the 2-D bend-over scale λ_2 is one half the slab bend-over scale λ_s for calculating the parallel mean free path, in place of one tenth of λ_s which was commonly assumed in the past. According to new results from multispacecraft measurements [*Weygand et al.*, 2009], for the slow wind the ratio of slab to 2-D correlation scales is around 2.6 (more 2-D-like) while in the fast wind (much less well determined due to lack of data) the ratio is around 0.7 (i.e., more slab-like). Therefore we choose $\lambda_s/\lambda_2 = 2$ in this paper.

[10] 4. This work uses a different energy ratio $\langle \delta b_s^2 \rangle / \langle \delta b_2^2 \rangle$ tailored to produce a power spectrum ratio of 0.15 in the inertial range (which is what *Bieber et al.* [1996] actually derived), where $\langle \delta b_s^2 \rangle$ is the mean of the variance of the slab geometry fluctuation, $\langle \delta b_2^2 \rangle$ the two-dimensional turbulent fluctuation. When the bend-over scales, λ_2 and λ_s, are the same, the two assumptions (energy ratio versus power spectrum ratio) are approximately equivalent. However when the length scales are substantially different, this is no longer true. In this circumstance, it is the power spectrum ratio that should be set to 0.15, not the energy ratio as was commonly assumed in prior work (including our prior work).

[11] 5. Much past work on particle transport in 2-D magnetic turbulence has employed a model 2-D spectrum with somewhat pathological characteristics such as an infinite correlation scale. Here we employ the model 2-D spectrum introduced by *Matthaeus et al.* [2007], which has an arbitrary power law behavior at long wavelengths. We consider spectrum models ranging from the somewhat pathological one commonly used in the past, to completely well behaved models consistent with strictly homogeneous turbulence.

[12] 6. The work of *Zank et al.* [1998] employed the BAM [*Bieber and Matthaeus*, 1997] model for the perpendicular diffusion coefficient. Here we employ the NLGC theory which has been shown to be consistent both with direct numerical simulations and with key observational constraints on the perpendicular diffusion coefficient [*Bieber et al.*, 2004].

[13] This paper is constructed as follows: The calculation of cosmic ray diffusion coefficients is presented in section 2. The turbulence model is briefly discussed in section 3. Our results are presented in section 4 and are compared with published observations from Helios, Voyager 2, and Ulysses. Finally, section 5 is our conclusion.

2. Cosmic Ray Mean Free Paths

[14] The cosmic ray diffusion tensor, κ_{ij}, can be written as

$$\kappa_{ij} = \kappa_\perp \delta_{ij} + \frac{B_i B_j}{B^2}\left(\kappa_\parallel - \kappa_\perp\right) + \epsilon_{ijk}\kappa_A \frac{B_k}{B}, \tag{1}$$

where B_i, B_j, and B_k are the mean magnetic field components, δ_{ij} is the Kronecker delta tensor, and ϵ_{ijk} is the alternating tensor, with value zero unless i, j, k are all different, in which case the value is 1 or -1 if i, j, k are or are not in cyclic order. The parameter $\kappa_\parallel$ is the parallel diffusion coefficient, $\kappa_\perp$ is the perpendicular diffusion coefficient, and κ_A denotes the antisymmetric component of the diffusion tensor, the divergence of which is the drift velocity. Finally, B is the mean magnetic field strength [*Parker*, 1958]

$$B = B_0\left(\frac{R_0}{r}\right)^2\left[1 + \left(\frac{\Omega \sin\theta}{U}\right)^2 (r - R_0)^2\right]^{1/2}, \tag{2}$$

where R_0 is the source surface radius which is taken to be 20 solar radii, r is the radial distance from the Sun, θ is the polar angle, Ω is the solar rotation rate which is based on a period of 25.4 days, and B_0 is the magnetic field strength on the source surface. U is the radial solar wind speed which is a function of θ (see Figure 1) and is constant as a function of heliocentric distance.

[15] If we define ψ as the angle between the mean magnetic field and the radial direction

$$\tan\psi = \frac{\Omega \sin\theta}{U}(r - R_0). \tag{3}$$

Thus, the radial diffusion coefficient, κ_r, can be rewritten as

$$\kappa_{rr} = \kappa_\perp \sin^2\psi + \kappa_\parallel \cos^2\psi, \tag{4}$$

which is important for solar modulation. Its value is also calculated and discussed in section 4 along with $\kappa_\parallel$ and $\kappa_\perp$. In this paper we define mean free paths $\lambda_{\parallel,\perp}$ in the same

way as *Zank et al.* [1998], $\lambda_{\parallel,\perp} \equiv 3\kappa_{\parallel,\perp}/v$, where v is the particle speed.

2.1. Parallel Mean Free Path

[16] Observations [*Palmer*, 1982; *Bieber et al.*, 1994] show that a pure "slab" model of interplanetary magnetic turbulence [*Jokipii*, 1966] is inadequate to describe parallel diffusion. In the slab model the turbulent fluctuations are perpendicular to the mean magnetic field, and the associated wave vectors are parallel to the mean magnetic field. Observed parallel mean free paths are generally much larger than the "slab" model prediction. On the other hand, recent evidence suggests that interplanetary magnetic turbulence is well described by a composite model comprising a dominant two-dimensional component (70% to 90%) and a minor slab component [*Matthaeus et al.*, 1990; *Bieber et al.*, 1996]. As outlined by *Bieber et al.* [1995] and *Zank et al.* [1998], the parallel mean free path for the composite model is approximated by

$$\lambda_{\parallel} = 3.1371 \frac{B^{5/3}}{b_{x,slab}^2} \left(\frac{P}{c}\right)^{1/3} \lambda_{slab}^{2/3} \times \left[1 + \frac{7/9A}{(1/3+q)(q+7/3)}\right]. \quad (5)$$

Here

$$R_L = \frac{P}{Bc}, \quad (6)$$

$$s = 0.746834 \frac{R_L}{\lambda_{slab}}, \quad (7)$$

$$A = \left(1+s^2\right)^{5/6} - 1, \quad (8)$$

$$q = \frac{5s^2/3}{1+s^2-\left(1+s^2\right)^{1/6}}, \quad (9)$$

where c is the speed of light, R_L the particle Larmor radius, $b_{x,slab}^2$ the variance of the x component of the slab geometry fluctuation, P the particle rigidity, λ_{slab} the correlation length for slab turbulence, and B the mean magnetic field magnitude determined by equation (2). This formula is valid from 10 MV to 10 GV and is very close to the exact Fokker-Planck result [*Bieber et al.*, 1995].

2.2. Perpendicular Mean Free Path

[17] Quasi-linear theory (QLT) for slab geometry has a restriction that limits its application to high energies [*Jokipii*, 1966; *Forman*, 1977]. For particles with Larmor radius close to or smaller than the parallel turbulence correlation scale, diffusion is much weaker (i.e., the diffusion coefficient is smaller) than QLT predicts. On the contrary, based on Taylor-Green-Kubo formulation, *Bieber and Matthaeus* [1997] presents a theory ("BAM") that is weaker than QLT and underestimates the diffusion. As shown by *Bieber et al.* [2004] the nonlinear guiding center (NLGC) theory shows good agreement with observations of Jovian electrons [*Chenette et al.*, 1977] and of Galactic protons [*Heber et al.*, 1996; *Burger et al.*, 2000]. The QLT and BAM results bracket the NLGC results.

[18] According to the NLGC theory [*Matthaeus et al.*, 2003], the relation between $\lambda_\perp$ and $\lambda_\parallel$ is

$$\lambda_\perp = \lambda_\parallel \frac{a^2}{B^2} \int_{-\infty}^{\infty} \frac{S_{xx}(\mathbf{k})}{1 + k_\perp^2 \lambda_\parallel \lambda_\perp/3 + k_z^2 \lambda_\parallel^2/3} d^3\mathbf{k}, \quad (10)$$

where a^2 is 1/3, $\mathbf{k}$ the wave vector, $S_{xx}(\mathbf{k})$ the turbulent fluctuation spectrum, and $k_\perp = \sqrt{k_x^2 + k_y^2}$. Here k_x, k_y, and k_z are components of $\mathbf{k}$, and the z direction is defined to be the mean field direction.

[19] We note that equation (10) is valid only for the case of turbulence with full 3-D structure, i.e., the turbulence correlation function depends explicitly on all three spatial coordinates. The equation is not valid for the case of reduced dimensionality turbulence which has one or more ignorable spatial coordinates, such as pure slab turbulence, because analytical studies have shown that particles are tied to individual field lines in this case [*Jokipii et al.*, 1993; *Kóta and Jokipii*, 2000]. However, the turbulence model used here, a combination of slab and 2-D turbulence, has no ignorable coordinates, and use of the NLGC model is justified.

[20] For one-dimensional slab turbulence with a fluctuation $\mathbf{b}_s$ perpendicular to the mean field, the power spectrum S_s can be expressed as [*Matthaeus et al.*, 2007]

$$S_s(k \le 1/\lambda_s) = C_s \langle b_s^2 \rangle \lambda_s, \quad (11)$$

$$S_s(k > 1/\lambda_s) = C_s \langle b_s^2 \rangle \lambda_s (k\lambda_s)^{-\nu}, \quad (12)$$

where C_s is a normalization constant, $k = |k_z|$, λ_s is the slab bend-over scale, and $S_s(k)$ is the one-dimensional slab turbulent fluctuation spectrum. The index ν is set to be 5/3, corresponding to the Kolmogorov spectrum in the inertial range. By the fact that $2\int_0^\infty dk S_s(k) = \langle b_s^2 \rangle$, we determine that $C_s = 1/5$.

[21] A two-dimensional axisymmetric turbulent fluctuation spectrum can be written as [*Matthaeus et al.*, 2007]

$$S_2(k \le 1/\lambda_2) = C_2 \langle b_2^2 \rangle \lambda_2^2 (\lambda_2 k)^p, \quad (13)$$

$$S_2(k > 1/\lambda_2) = C_2 \langle b_2^2 \rangle \lambda_2^2 (\lambda_2 k)^{-\nu-1}, \quad (14)$$

where C_2 is a normalization constant, $k = k_\perp$, λ_2 is the 2-D bend-over scale, and $S_2(k)$ is the two-dimensional axisymmetric turbulent fluctuation spectrum. The power index p can be −1, 0, 1, or 2. The integral values of p correspond to different power spectra as discussed by *Matthaeus et al.* [2007]. Specifically, the value $p = 2$ is appropriate for strictly homogeneous turbulence, while all values $p \ge 1$ have both a finite ultrascale and finite correlation scale. The value $p = 0$ has a finite correlation scale but infinite ultrascale, while for $p = -1$, both the correlation scale and ultrascale are infinite. We note that much prior work in this area employed a 2-D spectrum model that corresponds to the somewhat pathological $p = -1$ spectrum. The value of ν is taken to be 5/3 as in the one-dimensional case, and $\mathbf{b}_2$ is the two-dimensional turbulent fluctuation. Depending on the value of p, C_2 takes different values as shown in Table 1 determined by normalization.

Table 1. Values of C_2 and $\langle b_s^2\rangle/\langle b_2^2\rangle$ for Different Turbulent Spectra

p	$\pi\ C_2$	$\langle b_s^2\rangle/\langle b_2^2\rangle$	$\langle b_s^2\rangle/\langle b_2^2\rangle$ for $\nu = 5/3$
−1	$0.5\ (\nu-1)/\nu$	$\frac{3}{17}\frac{1}{\sqrt{\pi}}\frac{\nu\Gamma(\nu/2)}{\Gamma(\nu/2+0.5)}\frac{1}{\nu}2^{\nu-1}$	0.1998
0	$(\nu-1)/(\nu+1)$	$\frac{3}{17}\frac{1}{\sqrt{\pi}}\frac{\nu\Gamma(\nu/2)}{\Gamma(\nu/2+0.5)}\frac{2}{1+\nu}2^{\nu-1}$	0.2497
1	$1.5(\nu-1)/(\nu+2)$	$\frac{3}{17}\frac{1}{\sqrt{\pi}}\frac{\nu\Gamma(\nu/2)}{\Gamma(\nu/2+0.5)}\frac{3}{2+\nu}2^{\nu-1}$	0.2724
2	$2(\nu-1)/(\nu+3)$	$\frac{3}{17}\frac{1}{\sqrt{\pi}}\frac{\nu\Gamma(\nu/2)}{\Gamma(\nu/2+0.5)}\frac{4}{3+\nu}2^{\nu-1}$	0.2854

[22] Using equations (11)–(14), we obtain the formula for $\lambda_\perp$ by employing Kronecker delta function, $\delta_{p,n}$, to serve as a switch for different p values

$$\begin{aligned}\lambda_\perp = {} & \frac{a^2 C_s\langle b_s^2\rangle}{B^2}\sqrt{3}\lambda_s \tan^{-1}\frac{\lambda_\parallel}{\sqrt{3}\lambda_s} \\ & + \frac{a^2 C_s\langle b_s^2\rangle}{B^2}\frac{9}{8}\frac{\lambda_s^2}{\lambda_\parallel}{}_2\mathrm{F}_1\left(1;\frac{4}{3};\frac{7}{3};-\frac{3\lambda_s^2}{\lambda_\parallel^2}\right) \\ & + \frac{a^2\pi C_2\langle b_2^2\rangle}{B^2}\left\{\frac{9}{8}\frac{3\lambda_2^2}{\lambda_\perp}{}_2\mathrm{F}_1\left(1;\frac{4}{3};\frac{7}{3};-\frac{3\lambda_2^2}{\lambda_\parallel\lambda_\perp}\right)\right. \\ & + \delta_{p,-1}\frac{\sqrt{3}\lambda_2\sqrt{\lambda_\parallel}}{\sqrt{\lambda_\perp}}\tan^{-1}\frac{\sqrt{\lambda_\parallel\lambda_\perp}}{\sqrt{3}\lambda_2} \\ & + \delta_{p,0}\frac{3\lambda_2^2}{2\lambda_\perp}\log\left(1+\frac{\lambda_\parallel\lambda_\perp}{3\lambda_2^2}\right) \\ & + \delta_{p,1}\frac{3\lambda_2^2}{\lambda_\perp}\left(1-\frac{\sqrt{3}\lambda_2}{\sqrt{\lambda_\parallel\lambda_\perp}}\tan^{-1}\frac{\sqrt{\lambda_\parallel\lambda_\perp}}{\lambda_2\sqrt{3}}\right) \\ & \left. + \delta_{p,2}\frac{3\lambda_2^2}{2\lambda_\perp}\left[1-\frac{3\lambda_2^2}{\lambda_\parallel\lambda_\perp}\ln\left(1+\frac{\lambda_\parallel\lambda_\perp}{3\lambda_2^2}\right)\right]\right\}, \end{aligned} \tag{15}$$

where ${}_2\mathrm{F}_1$ is a hypergeometric function. Note that the expression for $\lambda_\perp$ is in an implicit form. So a numerical iterative method is used to obtain it.

3. Turbulence Model

[23] After major simplifications, the full set of MHD transport equations can be reduced to four equations including key physical processes such as turbulence decay, solar wind expansion, turbulence driving by stream shear and by pickup ions [*Marsch and Tu*, 1989, 1990a, 1990b; *Zhou and Matthaeus*, 1990a, 1990b; *Tu and Marsch*, 1993; *Matthaeus et al.*, 1994, 1996, 2004; *Oughton and Matthaeus*, 1995; *Zank et al.*, 1996, 1998]. The most recent and complete derivation is presented in detail by *Breech et al.* [2008]. In this section, we just outline the major points in this model.

[24] Following the same notation as *Breech et al.* [2008], we decompose the velocity and the magnetic field into two components

$$\mathbf{V} = \langle\mathbf{V}\rangle + \mathbf{v}, \tag{16}$$

$$\mathbf{B} = \langle\mathbf{B}\rangle + \mathbf{b}, \tag{17}$$

where $\langle\cdots\rangle$ denotes an appropriate average operator and where $\mathbf{v}$ and $\mathbf{b}$ are the fluctuating components. For convenience, we use Elsässer variables, $\mathbf{z}^\pm \equiv \mathbf{v} \pm \mathbf{b}/\sqrt{4\pi\rho}$ [*Elsässer*, 1950], where ρ is the (proton) mass density. The governing equation for inward and outward propagating modes is

$$\begin{aligned}&\frac{\partial\mathbf{z}^\pm}{\partial t} + (\mathbf{U}\mp\mathbf{V}_A)\cdot\nabla\mathbf{z}^\pm + \frac{1}{2}\nabla\cdot\left(\frac{\mathbf{U}}{2}\pm\mathbf{V}_A\right)\mathbf{z}^\pm \\ &\quad + \mathbf{z}^\pm\cdot\left[\nabla\mathbf{U}\pm\frac{\nabla\mathbf{B}_0}{\sqrt{4\pi\rho}} - \frac{I}{2}\nabla\cdot\left(\frac{\mathbf{U}}{2}\pm\mathbf{V}_A\right)\right] \\ &= \mathbf{N}\mathbf{L}^\pm + \mathbf{S}^\pm\ , \end{aligned} \tag{18}$$

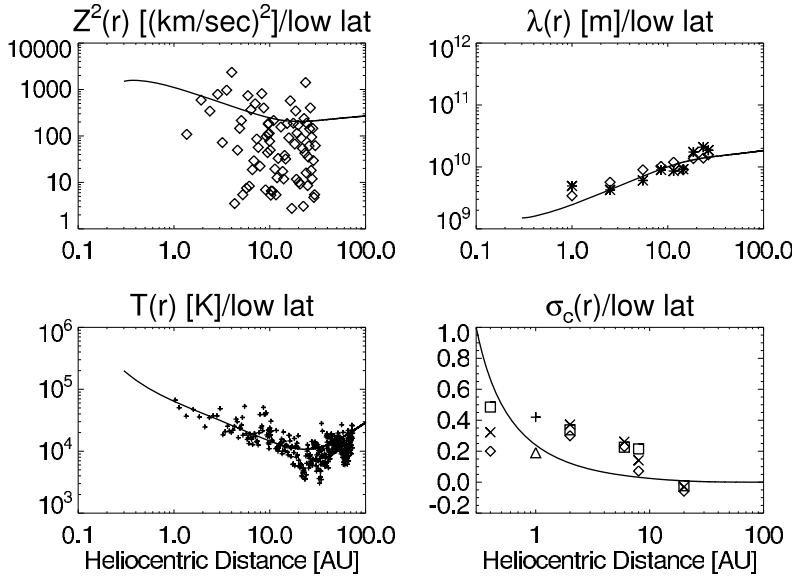

Figure 2. Solution 1 for the turbulence model in the ecliptic plane. Observational data are from Voyager 2, Helios, and Omni. Solid lines are our simulations. The Z^2 data is from *Zank et al.* [1996]. The temperature, T, data comes from *Smith et al.* [2001]. The correlation length, λ, data is also from *Smith et al.* [2001]. The diamonds and the stars denote different methods for calculating. The σ_c data comes from *Roberts et al.* [1987], except for the points at 1 AU. Those were ones we computed from Omni data (pluses and triangles). The different symbols correspond to different averaging intervals (crosses are for an averaging interval of 7 hours, squares are for an averaging interval of 3 hours, and diamonds are for an averaging interval of 27 hours).

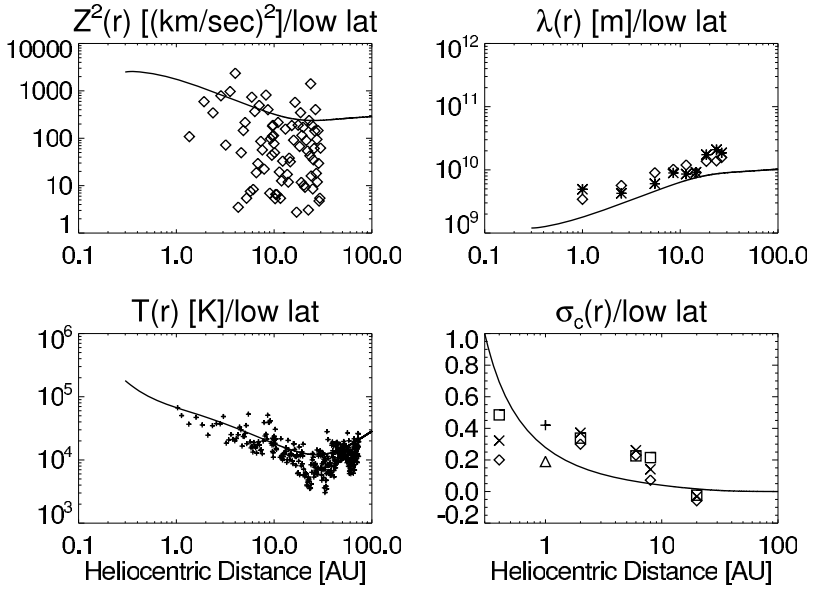

Figure 3. Solution 2 for the turbulence model in the ecliptic plane. Observational data are from Voyager 2, Helios, and Omni. Symbols are the same as in Figure 2.

where $\mathbf{U} \equiv \langle \mathbf{V} \rangle$, $\mathbf{B}_0 \equiv \langle \mathbf{B} \rangle$, $\mathbf{V}_A \equiv \mathbf{B}_0/\sqrt{4\pi\rho}$, and I is the identity matrix. **NL** stands for nonlinear effects and **S** stands for source terms.

[25] The total energy for both inward and outward modes is

$$Z^2 = \frac{Z_+^2 + Z_-^2}{2} = \frac{\langle |\mathbf{z}^+|^2 + |\mathbf{z}^-|^2 \rangle}{2} = \langle |\mathbf{v}|^2 + |\mathbf{b}|^2/(4\pi\rho) \rangle. \quad (19)$$

The normalized cross helicity is defined as

$$\sigma_c = \frac{H_c}{E} = \frac{Z_+^2 - Z_-^2}{Z_+^2 + Z_-^2}, \quad (20)$$

where $H_c = \langle \mathbf{v} \cdot \mathbf{b} \rangle$ is the actual cross helicity. The similarity scale λ can be associated with a correlation scale of the turbulence, for example,

$$\lambda = \int_0^\infty R(\zeta, 0, 0) d\zeta / R(0, 0, 0), \quad (21)$$

where R can be the trace of any one of the turbulence correlation tensors, $R = \langle \mathbf{v} \cdot \mathbf{v}' + \mathbf{b} \cdot \mathbf{b}' \rangle$ in this article. Here prime denotes evaluation at the lagged small-scale coordinate, e.g., $\mathbf{v}' = \mathbf{v}(\mathbf{r}, \mathbf{x} + \boldsymbol{\zeta})$ where $\boldsymbol{\zeta}$ denotes the lag. From equation (18), we derive equations for the evolution of $R^\pm$.

[26] Applying several assumptions relevant to solar wind, such as $U \gg V_A$, to equation (18), we can obtain the following transport model (see *Breech et al.* [2008] for details on the derivation):

$$\frac{dZ^2}{dr} = \frac{C_{sh} - M\sigma_D - 1}{r} Z^2 + \frac{\dot{E}_{PI}}{U} - \frac{\alpha f^+(\sigma_c)}{\lambda U} Z^3, \quad (22)$$

$$\frac{d\lambda}{dr} = \frac{\beta f^+(\sigma_c)}{U} Z - \frac{\beta}{\alpha} \frac{\dot{E}_{PI}}{UZ^2} \lambda, \quad (23)$$

$$\frac{d\sigma_c}{dr} = -\frac{C_{sh} - M\sigma_D}{r} \sigma_c + \frac{\alpha f'(\sigma)}{U\lambda} Z - \frac{\dot{E}_{PI}}{UZ^2} \sigma_c, \quad (24)$$

$$\frac{dT}{dr} = -\frac{4T}{3r} + \frac{m_p}{3k_B} \frac{\alpha}{U} f^+(\sigma_c) \frac{Z^3}{\lambda}. \quad (25)$$

where we define

$$f^\pm = \frac{(1 - \sigma_c^2)^{1/2}}{2} \left[(1 + \sigma_c)^{1/2} \pm (1 - \sigma_c)^{1/2} \right] \quad (26)$$

and

$$f'(\sigma) = \sigma_c f^+(\sigma_c) - f^-(\sigma_c) \quad (27)$$

for simplicity.

[27] In the above equations, m_p is the proton mass and k_B is Boltzmann's constant. The parameter $\sigma_D = -1/3$ describes the energy difference between the velocity and magnetic fields, and it is related to the Alfvén ratio, which is assumed to be 1/2. The parameter $M = 1/2$ is a geometric term relating to the underlying turbulence geometry, $C_{\rm sh}$ represents shear driving effects, and the $\dot{E}_{PI}$ terms account for the energy injected into the turbulence through wave-particle interactions of pickup protons (see *Williams et al.* [1995] and *Smith et al.* [2001] for the form of $\dot{E}_{PI}$). Finally, $\alpha = 2\beta$ are *de Kármán and Howarth*'s [1938] phenomenological constants. Note that the temperature equation includes heating through the turbulent dissipation term proportional to Z^3/λ.

4. Results

[28] Equations (22)–(25) can be solved by the Runge-Kutta method with appropriate initial conditions [*Breech et*

Table 2. Parameters and Initial Conditions in Equatorial Plane

	Case 1[a]	Case 2[a]	Case 3[a]	Solution 1	Solution 2
α	0.8	0.8	0.8	0.25	0.125
β	0.4	0.4	0.4	0.125	0.0625
C_{sh}	1	1	1	1.4	1.2
Z_0^2 (km/s)^2	3000	500	6000	1200	2000
λ_0 (AU)	0.008	0.008	0.015	0.01	0.008
σ_{c0}	0.6	0.6	0.6	1	1
T_0 (K)	180,000	180,000	300,000	200,000	180,000

[a] *Breech et al.* [2008].

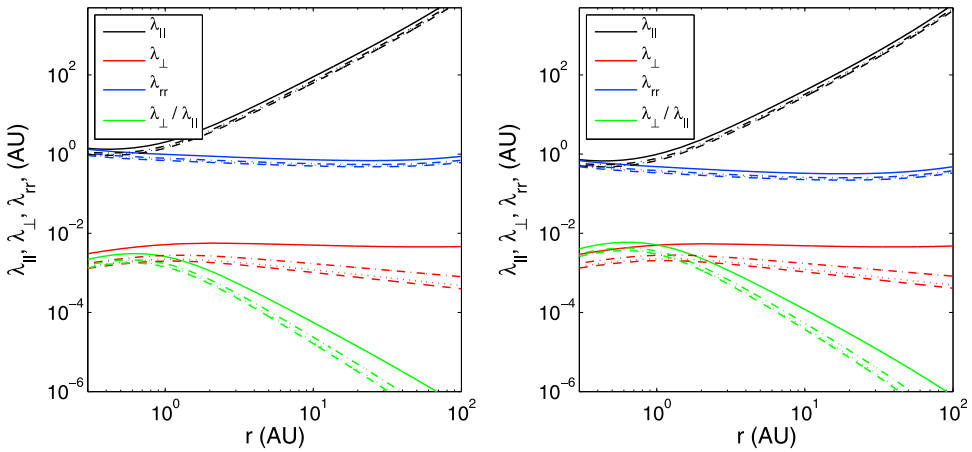

Figure 4. Parallel, perpendicular, and radial mean free paths for an undriven turbulence model ((left) Solution 1 and (right) Solution 2) in the ecliptic plane. Proton rigidity is 445 MV (100 MeV proton). Solid lines are for $p = -1$, dash-dotted lines are for $p = 0$, dotted lines are for $p = 1$, and dashed lines are for $p = 2$.

al., 2008]. The results are also calibrated with available spacecraft (Voyager 2, Helios, and Omni) data sets (see Figures 2 and 3). The solutions from this turbulence model provide us with Z^2 and λ values. We can convert the Z^2 to $\langle b_2^2 \rangle$ using the Alfvén ratio (assumed to be 1/2). We identify also $\lambda_2 = \lambda$. However, we must make an assumption about λ_s and $\langle b_s^2 \rangle$ to use equations (5), (15), and (4) to determine parallel, perpendicular, and radial mean free paths, respectively. In this paper, we assume that λ_s is twice λ_2 [*Weygand et al.*, 2009] and the ratio between $\langle b_2^2 \rangle$ and $\langle b_s^2 \rangle$ is determined by setting the ratio between the 2-D energy spectrum to 1-D slab energy spectrum as 85% to 15%. It is easy to show that

$$\frac{S_s}{S_2} = \frac{15}{85} = \frac{\Gamma\left(\frac{1+\nu}{2}\right)\sqrt{\pi}(1+p+\nu)}{\Gamma\left(\frac{\nu}{2}\right)\nu(p+2)} \frac{\langle b_s^2 \rangle}{\langle b_2^2 \rangle} \left(\frac{\lambda_s}{\lambda_2}\right)^{1-\nu}. \tag{28}$$

So the ratio between $\langle b_2^2 \rangle$ and $\langle b_s^2 \rangle$ is a function of p.

[29] We observe that our procedure of setting the inertial range energy spectrum 2-D:Slab in the ratio 85:15 is in contrast to prior work (including some of our own) which set the total turbulent energy 2-D:Slab in the ratio 85:15, or more commonly 80:20. The two assumptions are roughly equivalent when the 2-D and slab bend-over scales are the same, but they can give divergent results when the bend-over scales are different. Because the observational results of *Bieber et al.* [1996] apply to the energy spectrum in the inertial range, not the total energy, we believe our new approach is more consistent with available observational constraints.

[30] We choose two solutions of the turbulence model to show the characteristics of cosmic ray mean free paths and their sensitivity to modest variations of the turbulence properties. Solution 1, which is shown in Figure 2, displays a moderate similarity length scale, a moderate proton temperature, a moderate helicity, and a little bit higher-energy

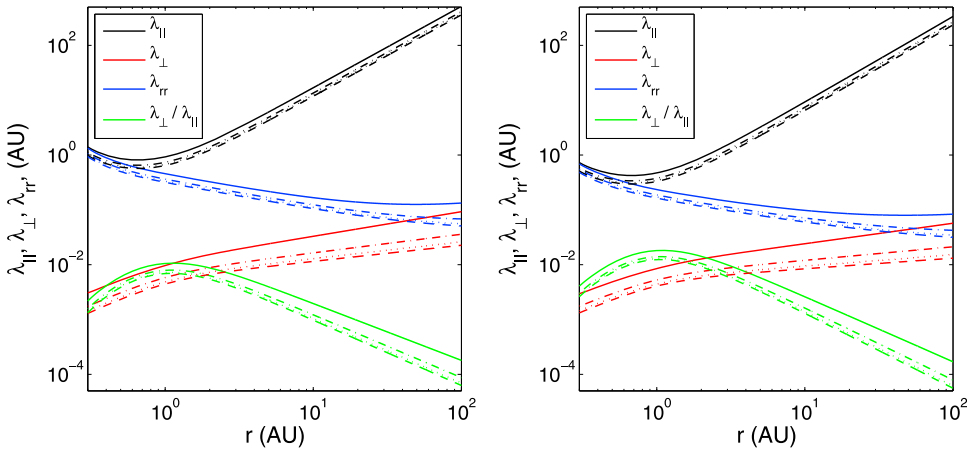

Figure 5. Parallel, perpendicular, and radial mean free paths for a stream-driven-only turbulence model ((left) Solution 1 and (right) Solution 2) in the ecliptic plane. Proton rigidity is 445 MV (100 MeV proton). Solid lines are for $p = -1$, dash-dotted lines are for $p = 0$, dotted lines are for $p = 1$, and dashed lines are for $p = 2$.

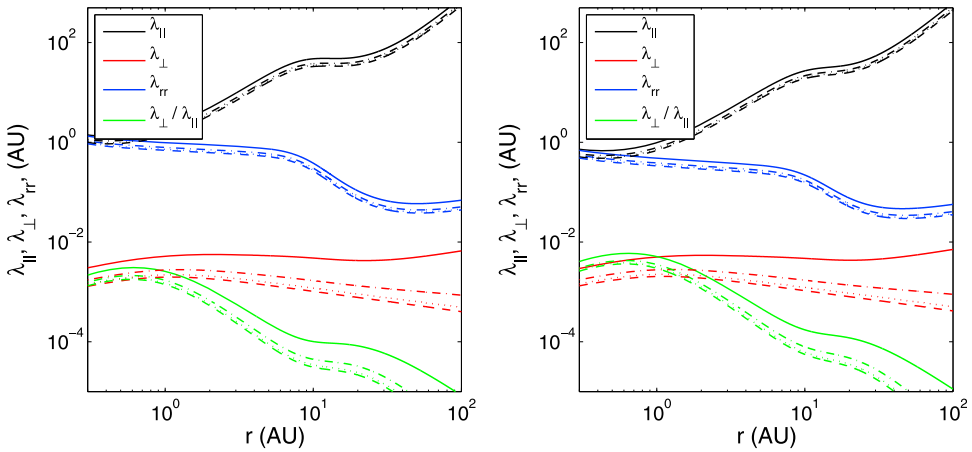

Figure 6. Parallel, perpendicular, and radial mean free paths for a pick-up-ion-driven-only turbulence model ((left) Solution 1 and (right) Solution 2) in the ecliptic plane. Proton rigidity is 445 MV (100 MeV proton). Solid lines are for $p = -1$, dash-dotted lines are for $p = 0$, dotted lines are for $p = 1$, and dashed lines are for $p = 2$.

density compared with the observations (though this impression is owing in part to the use of a logarithmic scale). Solution 2 (Figure 3) displays a smaller similarity length scale, a higher proton temperature, a larger helicity, and a higher-energy density compared with the observations. The parameters for Solution 1 and Solution 2 are listed in Table 2.

4.1. Radial Dependence of Mean Free Paths

[31] In Figures 4–7, we show parallel, perpendicular, and radial mean free paths (MFPs) for different driving mechanisms and for two solutions in the ecliptic plane. In Figure 4, we show parallel, perpendicular, and radial MFPs for the turbulence model without any driving force by setting $C_{sh} = 0$ and $\dot{E}_{PI} = 0$, which means it is a purely decaying MHD model. Clearly in Figure 4, the radial MFP, λ_{rr}, is dominated by the parallel MFP, $\lambda_{\|}$, because it is about 2 orders of magnitude larger than the perpendicular MFP, $\lambda_{\perp}$. The perpendicular MFP is almost a constant throughout the heliosphere, while the parallel MFP increases proportional to $r^{1.87}$ (Solution 1, regardless of p) or $r^{1.89}$ (Solution 2, regardless of p) beyond 1 AU. (The power index quoted here is obtained by assuming the lines are straight and using the data at 1 AU and at 100 AU. This method is used throughout this paper if not specified otherwise.) Because the angle ψ increases to almost 90° very fast according to equation (3), the radial MFP is almost a constant throughout the heliosphere for undriven turbulence. This result is different from *Zank et al.* [1998] who showed that λ_{rr} increases noticeably in the inner heliosphere. The reason for this difference is that in this paper, the correlation length increases monotonically with r while in *Zank et al.*'s [1998] study, the correlation length first goes down then goes up with r increasing. Solution 2 gives smaller $\lambda_{\|}$, therefore, smaller λ_{rr} than Solution 1. But the difference for $\lambda_{\perp}$ in these two solutions is negligible. From $p = -1$ to $p > 0$, $\lambda_{\perp}$ decreases to about 3 or 4 times smaller. For $\lambda_{\|}$, the difference is about

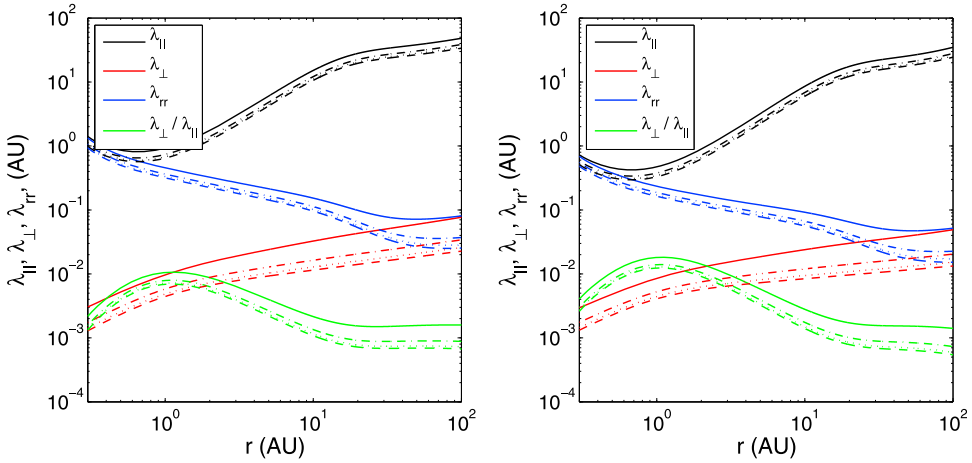

Figure 7. Parallel, perpendicular, and radial mean free paths for a fully driven turbulence model ((left) Solution 1 and (right) Solution 2) in the ecliptic plane. Proton rigidity is 445 MV (100 MeV proton). Solid lines are for $p = -1$, dash-dotted lines are for $p = 0$, dotted lines are for $p = 1$, and dashed lines are for $p = 2$.

Table 3. Parallel MFPs in AU for 100 MeV Protons at 1 AU

	Case 1[a]	Case 2[a]	Case 3[a]	Solution 1	Solution 2
$p = -1$	2.92	6.86	1.64	0.92	0.47
$p = 0$	2.33	5.49	1.31	0.74	0.38
$p = 1$	2.14	5.03	1.20	0.68	0.35
$p = 2$	2.04	4.80	1.15	0.64	0.33

[a]*Breech et al.* [2008].

50%. In any case, for $p = 1$ and $p = 2$, the difference is very small. Note that in this model, $\lambda_\perp/\lambda_\parallel$ is between 0.001 and 0.01 at 1 AU.

[32] In Figure 5, we show parallel, perpendicular, and radial MFPs for the turbulence model with only shear interaction by setting $\dot{E}_{PI} = 0$. In this case, the perpendicular MFP is much larger than it is in Figure 4, which means the shear interaction is important to enhance the perpendicular diffusion. The perpendicular MFP is no longer a constant, but increases proportional to $r^{0.35}$ ($p = 2$) or $r^{0.49}$ ($p = -1$) for Solution 1 and proportional to $r^{0.25}$ ($p = 2$) or $r^{0.41}$ ($p = -1$) for Solution 2. The parallel MFP increases proportional to $r^{1.37}$ (Solution 1, regardless of p) or $r^{1.43}$ (Solution 2, regardless of p), which is a much slower rate than the purely decaying MHD results. Therefore the radial MFP decreases throughout the heliosphere. In the outer heliosphere, it is evident that the contribution of the perpendicular MFP to the radial MFP is significant. In this case, $\lambda_\perp/\lambda_\parallel$ is of the order of 0.01 at 1 AU. So we can see from this comparison that shear interaction, or stream-driven turbulence is very effective to enhance perpendicular MFP.

[33] In Figure 6, we examine the pickup ion effect by setting $C_{sh} = 0$. It is obvious that the parallel MFP does not follow a power law any more due to the ionization effect, which starts at 10 AU. Before 10 AU, the calculated MFPs behave just like in Figure 4. Roughly to say, around 10–30 AU (which is also called ionization cavity), it is a transition region. Here we can define the inner heliosphere as the place before the ionization cavity, which is 10 AU. And we define the outer heliosphere as the place beyond the transition region, which is 30 AU. In this region, dissipation is enhanced due to the pick-up ions. Therefore all three MFPs decrease. Beyond 30 AU, the ion Larmor radius increases and the correlation scale λ_{slab} decreases. So $\lambda_\parallel$ increases again. In this case, the perpendicular MFP is insignificant as in Figure 4, it is about one thousandth of the parallel MFP. But still although the difference is very small, the perpendicular MFP is larger than in purely decaying MHD model. The radial MFP λ_{rr} is almost a constant beyond the ionization cavity for Solution 1 and Solution 2. Before the ionization cavity, λ_{rr} decreases very slowly.

[34] Finally, Figure 7 show the MFPs for a fully driven turbulence model with nonzero C_{sh} and $\dot{E}_{PI}$, which represents actual conditions in the solar wind. Because shear interaction and pickup ions both enhance the perpendicular diffusion, $\lambda_\perp$ is the largest of the four cases. Note that, when $r > 30$ AU,

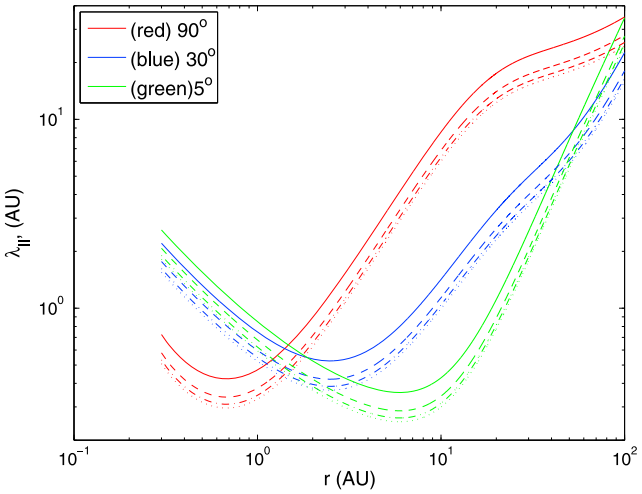

Figure 9. The radial dependence of the parallel MFP for different colatitudes for Solution 2. The solid line is $p = -1$. The dashed line is $p = 0$. The dash-dotted line is $p = 1$. The dotted line is $p = 2$.

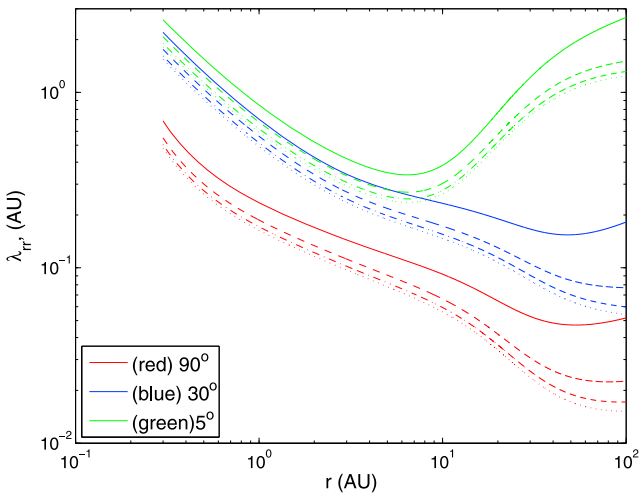

Figure 8. The radial dependence of the radial MFP for different colatitudes for Solution 2. The solid line is $p = -1$. The dashed line is $p = 0$. The dash-dotted line is $p = 1$. The dotted line is $p = 2$.

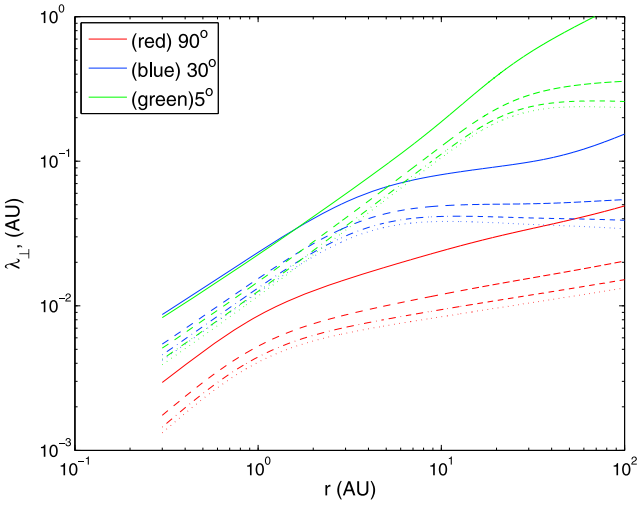

Figure 10. The radial dependence of the perpendicular MFP for different colatitudes for Solution 2. The solid line is $p = -1$. The dashed line is $p = 0$. The dash-dotted line is $p = 1$. The dotted line is $p = 2$.

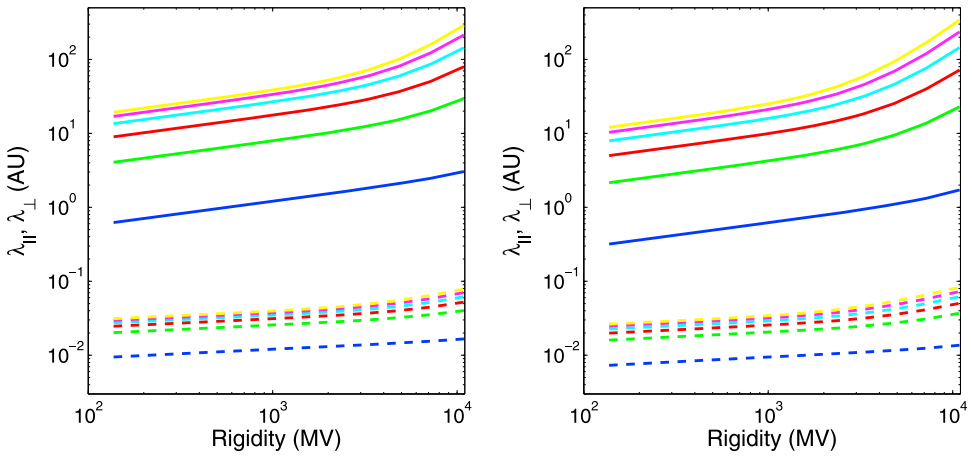

Figure 11. The rigidity dependence of the parallel and the perpendicular MFPs for (left) Solution 1 and (right) Solution 2 of the fully driven turbulent model when $p = -1$. Solid lines are for $\lambda_{||}$, and dashed lines are for $\lambda_{\perp}$. Colors from dark blue to yellow show radial distance at 1, 5, 9, 13, 17, and 21 AU.

$\lambda_{\perp}/\lambda_{||}$ is close to 0.0015 all the way to 100 AU. Generally, before the ionization cavity, $\lambda_{\perp}$ increases faster than it does in the outer heliosphere. For example, for $p = 2$, Solution 2, $\lambda_{\perp}$ is proportional to $r^{0.3}$ if $r < 10$ AU and $\lambda_{\perp}$ is proportional to $r^{0.2}$ if $r > 30$ AU. For $p = 2$, Solution 1, the indices are 0.4 and 0.3. Because pick-up ion driving mechanism and stream-driving mechanism both reduce λ_{rr}, λ_{rr} is smaller, especially in the outer heliosphere, where it remains nearly constant. In the inner heliosphere, λ_{rr} is $\sim r^{-0.5}$ for Solution 1 and $r^{-0.45}$ for Solution 2. In the inner heliosphere, $\lambda_{||}$ increases as $r^{1.22}$ (Solution 1) or $r^{1.26}$ (Solution 2) until 10 AU. In the outer heliosphere, $\lambda_{||}$ increases as $r^{0.31}$ (Solution 1) or $r^{0.40}$ (Solution 2). So we can still treat the region between 10 AU to 30 AU as a transition region. Another feature is that the perpendicular MFP plays a more important role in the outer heliosphere than in any other cases as a result of decreased $\lambda_{||}$ and increased $\lambda_{\perp}$.

[35] We close this subsection by considering the parallel mean free path for protons at 1 AU corresponding to the different solutions, and we compare these with "consensus" observational constraints [*Palmer*, 1982; *Bieber et al.*, 1994]. These values for 100 MeV protons at 1 AU for a fully driven turbulence model are listed in Table 3. We also present the MFPs calculated for case 1, case 2, and case 3 by *Breech et al.* [2008]. We point out here that case 1 is considered a better fit to the observational data. Case 2 and case 3 can be viewed as the upper bound and the lower bound. The Palmer consensus is that $\lambda_{||} \approx 0.08$–$0.3$ AU within the rigidity range 0.5–5000 MV. *Reames* [1999] suggests a larger MFP, around 1 AU, for protons. Generally speaking, these MFP values obtained by fitting the data depend upon models used by the authors. For example, for the same event, *Beeck et al.* [1987] finds $\lambda_{||} = 0.05$–0.1 AU, while *Mason et al.* [1991] gives $\lambda_{||} = 0.8$ AU. Here we find that $\lambda_{||}$ of case 3 from *Breech et al.* [2008] is close to 1 AU with higher temperature compared with observation, while case 1 and case 2 produce a too large $\lambda_{||}$ according to the consensus. The parallel MFP from Solution 1 and Solution 2 is closer to the upper limit of the consensus with a moderate temperature.

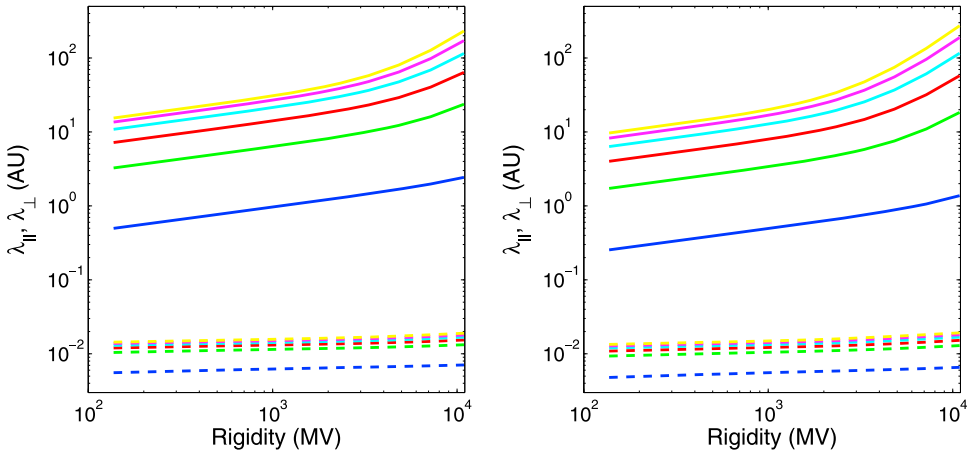

Figure 12. The rigidity dependence of the parallel and the perpendicular MFPs for (left) Solution 1 and (right) Solution 2 of the fully driven turbulent model when $p = 0$. Solid lines are for $\lambda_{||}$, and dashed lines are for $\lambda_{\perp}$. Colors from dark blue to yellow show radial distance at 1, 5, 9, 13, 17, and 21 AU.

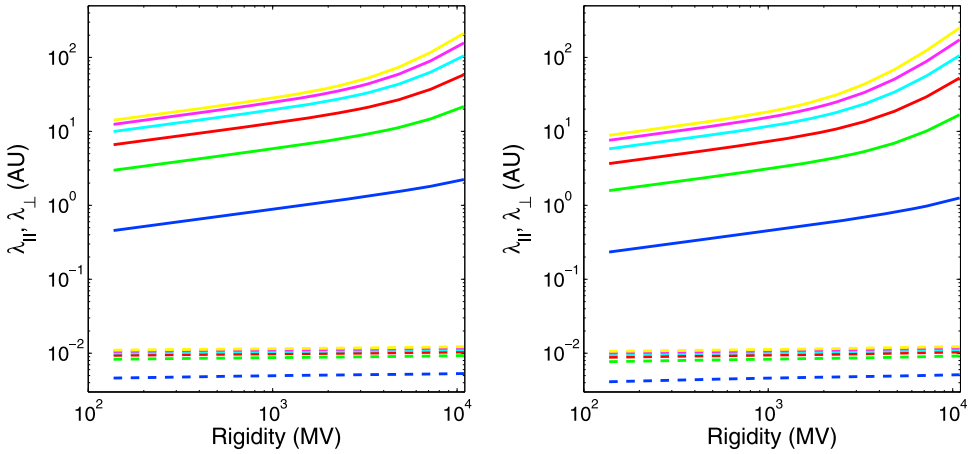

Figure 13. The rigidity dependence of the parallel and the perpendicular MFPs for (left) Solution 1 and (right) Solution 2 of the fully driven turbulent model when $p = 1$. Solid lines are for $\lambda_{||}$, and dashed lines are for $\lambda_{\perp}$. Colors from dark blue to yellow show radial distance at 1, 5, 9, 13, 17, and 21 AU.

4.2. Latitudinal Dependence of Mean Free Paths

[36] We present the MFPs at different latitude for a fully driven turbulence model in Figures 8–10 (we use Solution 2 as an example and change the boundary conditions along latitude.). Note the angles shown in Figures 8–10 are colatitude, or polar angle. So $\theta = 90°$ is the ecliptic plane. Each color denotes one particular latitude. Red is the ecliptic plane and green is $\theta = 5°$. Our assumption about the solar minimum solar wind is plotted in Figure 1. Near the equator, the solar wind speed is 380 km/s. At high latitudes, it is close to 800 km/s. Between $\theta = 10°$ to $\theta = 35°$, the solar wind speed increases linearly.

[37] In the ecliptic plane, λ_{rr} decreases as we have shown in Figure 7. But at high latitudes, λ_{rr} has a minimum at different radial locations depending on θ. Then it increases all the way to 100 AU. This is different from $\lambda_{\perp}$ which has no turning point. Perpendicular MFPs shown in Figure 10 increase monotonically from 1 AU to 100 AU. For parallel MFP, $\lambda_{||}$ has a minimum near 5 AU at high latitudes. It is obvious that $\lambda_{\perp}$ plays a more important role in determining λ_{rr} at high latitudes beyond 10 AU because not only $\lambda_{\perp}$ is in the same order as $\lambda_{||}$, the winding angle between the mean magnetic field and the radial direction goes almost to 90°. So although $\lambda_{||}$ decreases with latitude, λ_{rr} increases. We assume that the shear interaction is weaker near polar region and is stronger between $\theta = 10°$ to $\theta = 35°$. Therefore we expect that the behavior at high latitudes is different from ecliptic plane.

[38] One interesting feature in Figure 9 is that the parallel mean free path first decreases along radial direction inside 1 AU then increases in the equatorial plane. At other latitudes, the behavior is similar but the turning point is different. The reason for this is that the parallel mean free path depends on B and $b^2_{x,slab}$ (see equation (5)). As we know, B decreases proportional to $1/r^2$ when $r \ll 1$ AU, proportional to $1/r$ when $r \gg 1$ AU for a Parker field (see equation (2)). The variance of the x component of the slab fluctuation, $b^2_{x,slab}$ is proportional to Z^2 which is the output of the turbulent model. In Figure 3, we can see Z^2 decreases very slowly inside 1 AU then decreases much faster between 1 AU to 10 AU. Numerically speaking, $1/b^2_{x,slab}$ increases as

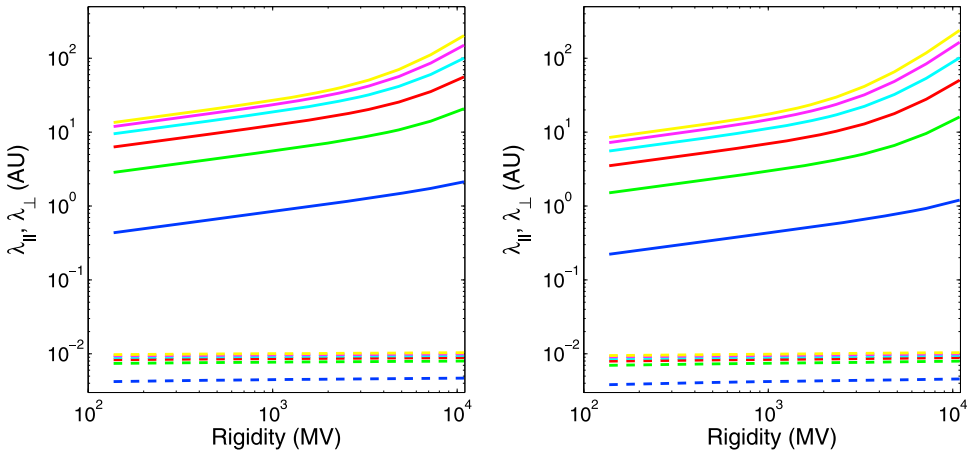

Figure 14. The rigidity dependence of the parallel and the perpendicular MFPs for (left) Solution 1 and (right) Solution 2 of the fully driven turbulent model when $p = 2$. Solid lines are for $\lambda_{||}$, and dashed lines are for $\lambda_{\perp}$. Colors from dark blue to yellow show radial distance at 1, 5, 9, 13, 17, and 21 AU.

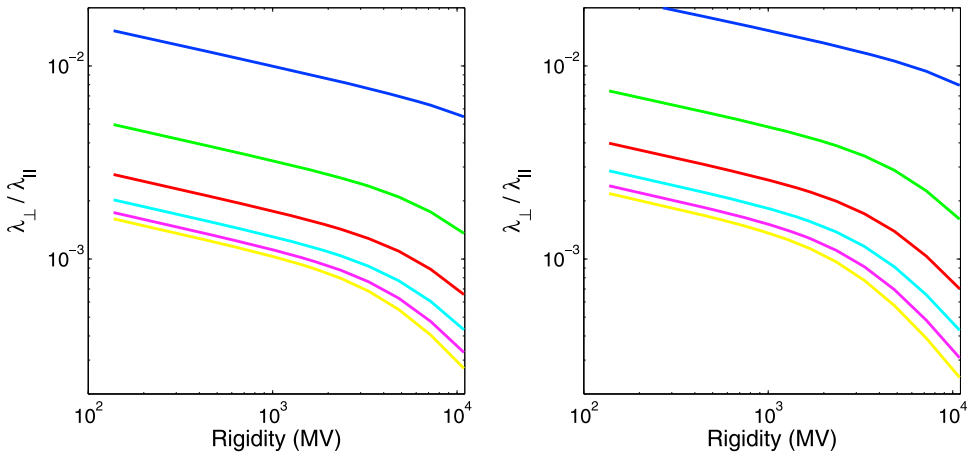

Figure 15. The rigidity dependence of the ratios of the parallel and the perpendicular MFPs for (left) Solution 1 and (right) Solution 2 of the fully driven turbulent when $p = -1$. Colors from dark blue to yellow show radial distance at 1, 5, 9, 13, 17, and 21 AU.

$r^{1.9}$ inside 1 AU, increases as $r^{2.5}$ before 10 AU, then increases as $r^{1.9}$ again beyond 10 AU. Thus this interesting behavior of $\lambda_\parallel$ is the result of a Parker field and our turbulence model.

4.3. Rigidity Dependence of Mean Free Paths

[39] In Figures 11–16, we show the rigidity dependence of the parallel and perpendicular MFPs for Solution 1 and Solution 2. The rigidity range is from 137 MV to about 11 GV (corresponding to 10 MeV to 10 GeV for protons). Figures 11–16 show that the p values, the choices of different spectrum, have little effect on the power index for the parallel mean free path. The rigidity dependence of the parallel mean free path is proportional to $P^{.404}$ for Solution 2 and $P^{.374}$ for Solution 1 at 1 AU from 0.1 GV to 10 GV, but in the outer heliosphere its dependence steepens above 4 GV; For both solutions, the rigidity dependence of the parallel MFP $\kappa_\parallel$ gradually steepens from $P^{1/3}$ at low rigidities to P^2 at high rigidities.

[40] For the perpendicular MFP, $\lambda_\perp$, except for $p = -1$, the dependence on rigidity is very weak. It is almost constant from 400 MV to 10 GV for all cases. But for $p = -1$, the perpendicular MFPs slowly increase with rigidity. For example, $p = -1$, for Solution 1, $\lambda_\perp$ increases from 0.01 AU at 500 MV to 0.015 AU at 10 GV. For Solution 2, it is from 0.085 AU to 0.014 GV in the same rigidity range.

5. Conclusions

[41] We present our analysis of $\lambda_\parallel$, $\lambda_\perp$, and λ_{rr} based on a recently developed MHD turbulence transport model, coupled with particle transport models based on quasi-linear theory ($\kappa_\parallel$) and the nonlinear guiding center theory ($\kappa_\perp$). This paper extends the research on MFPs by *Bieber* [1995] and *Zank et al.* [1998].

[42] The parallel MFP $\lambda_\parallel$ dominates in the inner heliosphere for all scenarios considered here. In the outer heliosphere, $\lambda_\perp$ plays a more and more important role in the stream-driven model and fully driven model, but remains relatively unimportant in the pick-up-ion-driven model and purely decaying MHD model. For the fully driven model, near the equator, λ_{rr} decreases from 1 AU to 10 AU almost

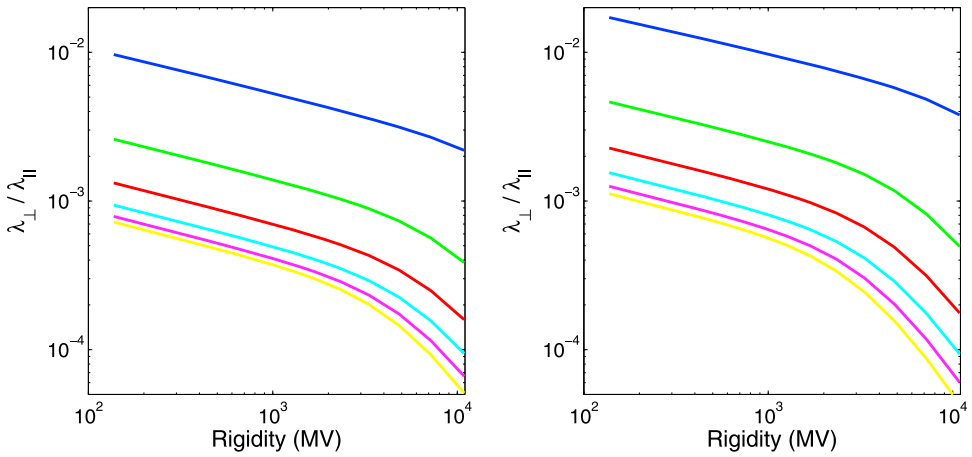

Figure 16. The rigidity dependence of the ratios of the parallel and the perpendicular MFPs for (left) Solution 1 and (right) Solution 2 of the fully driven turbulent when $p = 2$. Colors from dark blue to yellow show radial distance at 1, 5, 9, 13, 17, and 21 AU.

at a constant power law rate which is different from *Zank et al.* [1998]. In the outer heliosphere, the decreasing rate slows down almost completely. But in the polar region, λ_{rr} increases dramatically in the outer heliosphere, which qualitatively is consistent with *Zank et al.* [1998].

[43] The transition region (ionization cavity) shows the importance of the pickup ion effects. Both shearing effect and pickup ion effects enhance the role of the perpendicular MFP in the outer heliosphere. So in the fully driven model, the perpendicular MFP determines λ_{rr} when $r > 50$ AU. Our results show that the MFPs are much larger in the polar region than in the ecliptic plane, which partially is due to the weak shear interactions. So the particles can penetrate the heliosphere more easily in the polar region. The MFPs presented in this paper will be use in the ab initio model for cosmic ray transport [*Parhi et al.*, 2003; *Minnie*, 2006] which is under development.

[44] **Acknowledgments.** This work is supported by NASA Heliophysics Guest Investigator grant NNX07AH73G and by NASA Heliophysics Theory grant NNX08AI47G.

[45] Amitava Bhattacharjee thanks Jack Jokipii and another reviewer for their assistance in evaluating this paper.

References

Beeck, J., G. M. Mason, D. C. Hamilton, G. Wibberenz, H. Kunow, D. Hovestadt, and B. Klecker (1987), A multispacecraft study of the injection and transport of solar energetic particles, *Astrophys. J.*, *322*, 1052–1072.

Bieber, J. W. (1995), Cosmic rays in the heliosphere, *Int. Cosmic Ray Conf.*, *24*, 777–780.

Bieber, J. W., and W. H. Matthaeus (1997), Perpendicular diffusion and drift at intermediate cosmic-ray energies, *Astrophys. J.*, *485*, 655–659.

Bieber, J. W., W. H. Matthaeus, C. W. Smith, W. Wanner, M.-B. Kallenrode, and G. Wibberenz (1994), Proton and electron mean free paths: The Palmer consensus revisited, *Astrophys. J.*, *420*, 294–306.

Bieber, J. W., R. A. Burger, and W. H. Matthaeus (1995), The diffusion tensor throughout the heliosphere, *Int. Cosmic Ray Conf.*, *4*, 694–697.

Bieber, J. W., W. Wanner, and W. H. Matthaeus (1996), Dominant two-dimensional solar wind turbulence with implications for cosmic ray transport, *J. Geophys. Res.*, *101*, 2511–2522.

Bieber, J. W., W. H. Matthaeus, A. Shalchi, and G. Qin (2004), Nonlinear guiding center theory of perpendicular diffusion: General properties and comparison with observation, *Geophys. Res. Lett.*, *31*, L10805, doi:10.1029/2004GL020007.

Breech, B., W. H. Matthaeus, J. Minnie, J. W. Bieber, S. Oughton, C. W. Smith, and P. A. Isenberg (2008), Turbulence transport throughout the heliosphere, *J. Geophys. Res.*, *113*, A08105, doi:10.1029/2007JA012711.

Burger, R. A., M. S. Potgieter, and B. Heber (2000), Rigidity dependence of cosmic ray proton latitudinal gradients measured by the Ulysses spacecraft: Implications for the diffusion tensor, *J. Geophys. Res.*, *105*, 27,447–27,456.

Chenette, D. L., T. F. Conlon, K. R. Pyle, and J. A. Simpson (1977), Observations of Jovian electrons at 1 AU throughout the 13 month Jovian synodic year, *Astrophys. J.*, *215*, L95–L99.

de Kármán, T. v. (T. von Kármán), and L. Howarth (1938), On the statistical theory of isotropic turbulence, *Proc. R. Soc. London Ser. A*, *164*, 192–215.

Elsässer, W. M. (1950), The hydromagnetic equations, *Phys. Rev.*, *79*, 183–183.

Forman, M. A. (1977), The velocity correlation function in cosmic-ray diffusion theory, *Astrophys. Space Sci.*, *49*, 83–97.

Heber, B., et al. (1996), Spatial variation of >40 MeV/n nuclei fluxes observed during the ULYSSES rapid latitude scan, *Astron. Astrophys.*, *316*, 538–546.

Isenberg, P. A., C. W. Smith, and W. H. Matthaeus (2003), Turbulent heating of the distant solar wind by interstellar pickup protons, *Astrophys. J.*, *592*, 564–573.

Jokipii, J. R. (1966), Cosmic-ray propagation. Part I. Charged particles in a random magnetic field, *Astrophys. J.*, *146*, 480–487.

Jokipii, J. R., J. Kóta, and J. Giacalone (1993), Prependicular transport in 1- and 2-dimensional shock simulations, *Geophys. Res. Lett.*, *20*, 1759–1761.

Kóta, J., and J. R. Jokipii (2000), Velocity correlation and the spatial diffusion coefficients of cosmic rays: Compound diffusion, *Astrophys. J.*, *531*, 1067–1070.

Marsch, E., and C.-Y. Tu (1989), Dynamics of correlation functions with Elsasser variables for inhomogeneous MHD turbulence, *J. Plasma Phys.*, *41*, 479–491.

Marsch, E., and C.-Y. Tu (1990a), On the radial evolution of MHD turbulence in the inner heliosphere, *J. Geophys. Res.*, *95*, 8211–8229.

Marsch, E., and C.-Y. Tu (1990b), Spectral and spatial evolution of compressible turbulence in the inner solar wind, *J. Geophys. Res.*, *95*, 11,945–11,956.

Mason, G. M., D. V. Reames, and C. K. Ng (1991), Radial propagation of solar energetic particles assuming large scattering mean free paths in the interplanetary medium, *Int. Cosmic Ray Conf.*, *3*, 197–200.

Matthaeus, W. H., M. L. Goldstein, and D. A. Roberts (1990), Evidence for the presence of quasi-two-dimensional nearly incompressible fluctuations in the solar wind, *J. Geophys. Res.*, *95*, 20,673–20,683.

Matthaeus, W. H., Y. Zhou, G. P. Zank, and S. Oughton (1994), Transport theory and the WKB approximation for interplanetary MHD fluctuations, *J. Geophys. Res.*, *99*, 23,421–23,430.

Matthaeus, W. H., G. P. Zank, and S. Oughton (1996), Phenomenology of hydromagnetic turbulence in a uniformly expanding medium, *J. Plasma Phys.*, *56*, 659–675.

Matthaeus, W. H., G. P. Zank, C. W. Smith, and S. Oughton (1999), Turbulence, spatial transport, and heating of the solar wind, *Phys. Rev. Lett.*, *82*, 3444–3447.

Matthaeus, W. H., G. Qin, J. W. Bieber, and G. P. Zank (2003), Nonlinear collisionless perpendicular diffusion of charged particles, *Astrophys. J.*, *590*, L53–L56.

Matthaeus, W. H., J. Minnie, B. Breech, S. Parhi, J. W. Bieber, and S. Oughton (2004), Transport of cross helicity and radial evolution of Alfvénicity in the solar wind, *Geophys. Res. Lett.*, *31*, L12803, doi:10.1029/2004GL019645.

Matthaeus, W. H., J. W. Bieber, D. Ruffolo, P. Chuychai, and J. Minnie (2007), Spectral properties and length scales of two-dimensional magnetic field models, *Astrophys. J.*, *667*, 956–962.

Minnie, J. (2006), An ab initio approach to the heliospheric modulation of Galactic cosmic rays, Ph.D. thesis, North-West Univ., Potchefstroom, South Africa.

Oughton, S., and W. H. Matthaeus (1995), Linear transport of solar wind fluctuations, *J. Geophys. Res.*, *100*, 14,783–14,800.

Palmer, I. D. (1982), Transport coefficients of low-energy cosmic rays in interplanetary space, *Rev. Geophys. Space Phys.*, *20*, 335–351.

Parhi, S., J. W. Bieber, W. H. Matthaeus, and R. A. Burger (2003), Toward an ab initio theory of the solar modulation of cosmic rays, *Astrophys. J.*, *585*, 502–515.

Parker, E. N. (1958), Dynamics of the interplanetary gas and magnetic fields, *Astrophys. J.*, *128*, 664–676.

Reames, D. V. (1999), Particle acceleration at the Sun and in the heliosphere, *Space Sci. Rev.*, *90*, 413–491.

Roberts, D. A., L. W. Klein, M. L. Goldstein, and W. H. Matthaeus (1987), The nature and evolution of magnetohydrodynamic fluctuations in the solar wind: Voyager observations, *J. Geophys. Res.*, *92*, 11,021–11,040.

Smith, C. W., W. H. Matthaeus, G. P. Zank, N. F. Ness, S. Oughton, and J. D. Richardson (2001), Heating of the low-latitude solar wind by dissipation of turbulent magnetic fluctuations, *J. Geophys. Res.*, *106*, 8253–8272.

Tu, C.-Y., and E. Marsch (1993), A model of solar wind fluctuations with two components: Alfven waves and convective structures, *J. Geophys. Res.*, *98*, 1257–1276.

Weygand, J. M., W. H. Matthaeus, S. Dasso, M. G. Kivelson, L. M. Kistler, and C. Mouikis (2009), Anisotropy of the Taylor scale and the correlation scale in plasma sheet and solar wind magnetic field fluctuations, *J. Geophys. Res.*, *114*, A07213, doi:10.1029/2008JA013766.

Williams, L. L., G. P. Zank, and W. H. Matthaeus (1995), Dissipation of pickup-induced waves: A solar wind temperature increase in the outer heliosphere?, *J. Geophys. Res.*, *100*, 17,059–17,068.

Zank, G. P., W. H. Matthaeus, and C. W. Smith (1996), Evolution of turbulent magnetic fluctuation power with heliospheric distance, *J. Geophys. Res.*, *101*, 17,093–17,108.

Zank, G. P., W. H. Matthaeus, J. W. Bieber, and H. Moraal (1998), The radial and latitudinal dependence of the cosmic ray diffusion tensor in the heliosphere, *J. Geophys. Res.*, *103*, 2085–2097.

Zhou, Y., and W. H. Matthaeus (1990a), Transport and turbulence modeling of solar wind fluctuations, *J. Geophys. Res.*, *95*, 10,291–10,311.

Zhou, Y., and W. H. Matthaeus (1990b), Remarks on transport theories of interplanetary fluctuations, *J. Geophys. Res.*, *95*, 14,863–14,871.

J. W. Bieber, J. Clem, W. H. Matthaeus, and C. Pei, Bartol Research Institute, Department of Physics and Astronomy, University of Delaware, Newark, DE 19716, USA. (jwbieber@bartol.udel.edu; clem@bartol.udel.edu; whm@udel.edu; pei@bartol.udel.edu)

B. Breech, NASA Goddard Space Flight Center, Mail Code 673, Greenbelt, MD 20716, USA. (breech@cis.udel.edu)

R. A. Burger, Unit for Space Physics, School of Physics, North-West University, Potchefstroom Campus, Private Bag X6001, Potchefstroom 2520, South Africa. (adri.burger@nwu.ac.za)